Novel Methods for Predicting Photometric Redshifts from Broad Band Photometry using Virtual Sensors

M. J. Way

NASA Ames Research Center, Space Sciences Division, MS 245-6, Moffett Field, CA 94035, USA

A. N. Srivastava

NASA Ames Research Center, Intelligent Systems Division, MS 269-4, Moffett Field, CA 94035, USA

ABSTRACT

We calculate photometric redshifts from the Sloan Digital Sky Survey Main Galaxy Sample, The Galaxy Evolution Explorer All Sky Survey, and The Two Micron All Sky Survey using two new training-set methods. [1] We utilize the broad-band photometry from the three surveys alongside Sloan Digital Sky Survey measures of photometric quality and galaxy morphology. Our first training-set method draws from the theory of ensemble learning while the second employs Gaussian process regression both of which allow for the estimation of redshift along with a measure of uncertainty in the estimation. The Gaussian process models the data very effectively with small training samples of approximately 1000 points or less. These two methods are compared to a well known Artificial Neural Network training-set method and to simple linear and quadratic regression. We also demonstrate the need to provide confidence bands on the error estimation made by both classes of models. Our results indicate that variations due to the optimization procedure used for almost all neural networks, combined with the variations due to the data sample, can produce models with variations in accuracy that span an order of magnitude. A key contribution of this paper is to quantify the variability in the quality of results as a function of model and training sample. We show how simply choosing the "best" model given a data set and model class can produce misleading results. We also investigate supplemental information provided by the Sloan Digital Sky Survey photometric pipeline related to photometric quality and galaxy morphology tracers. We show that,

---

[1]This paper was submitted to Astrophysical Journal in December 2005.

using these additional quality and morphology indicators rather than only the Sloan Digital Sky Survey broad-band u,g,r,i,z imaging data commonly used, one can improve redshift accuracy by 10s of percent. Near Infrared j,h,k$_s$ broad-band photometry provided from the Two Micron All Sky Survey and near-ultraviolet and far-ultraviolet broad-band data from The Galaxy Evolution Explorer All Sky Survey are also investigated where they overlap with the Sloan Digital Sky Survey. Our results show that robust photometric redshift errors as low as 0.02 RMS can regularly be obtained. We believe these can be expanded to other photometric surveys where sufficient redshift calibration objects exist.

Subject headings: Photometric Redshifts, Sloan Digital Sky Survey, Galaxy Evolution Explorer All Sky Survey, Two Micron All Sky Survey

1. Introduction

Using broad-band photometry in multiple filters to estimate redshifts of galaxies was likely first attempted by Baum (1962) on 25 galaxies in nine broad-band imaging filters in the Visible and Near Infrared range. Given the low throughput of spectrographs much is to be gained by attempting to estimate galaxy redshifts from broad-band colors rather than from measurement of individual spectra. In the Sloan Digital Sky Survey (SDSS, York et al. 2000) 100 million galaxies will have accurate broad-band ugriz photometry, but only 1 million galaxy redshifts from this sample will be measured. If a method can be found to obtain an accurate estimate of the redshift for the larger SDSS photometric catalog, rather than the smaller spectroscopic one, much better constraints on the formation and evolution of large-scale structural elements such as galaxy clusters, filaments, and walls and cosmological models in general (e.g. Blake & Bridle 2005) may be achieved.

Two approaches, Spectral Energy Distribution fitting (SED fitting) also known as "template-fitting" and the training-set method (TS method), have been used to obtain photometric redshifts over the past 30 years. In order to use either method galaxies with a similar range in magnitude and color over the same possible redshift range must be used to estimate the redshifts from the broad-band colors measured. SED fitting has historically been the preferred method (e.g. Koo 1985; Loh & Spillar 1986; Lanzetta et al. 1996; Kodama et al. 1999; Benítez 2000; Babbedge et al. 2004; Padmanabhan et al. 2005) given the historically low numbers of galaxies with spectroscopically confirmed redshifts in photometric surveys of the universe.

There are many approaches to SED fitting. For example, Kodama et al. (1999) uses four

filter (BVRI) photometry and a Bayesian classifier using SED fitting which they have tested out to z=1 and claim is valid beyond this redshift. The approach of Benítez (2000) makes use of additional information such as the shape of the redshift distributions and fractions of different galaxy types. This may be helpful in instances where one has a limited sample size at large redshifts, but it may also bias an estimator by making assumptions which one cannot verify statistically.

TS methods rely on having a large enough sample of spectroscopic redshifts to represent the magnitudes and colors of the broad-band photometric sample. Hence these methods have been restricted to relatively nearby z<1 surveys, such as the SDSS, rather than much deeper surveys like the Hubble Deep Field (Williams et al. 1996) which have a paucity of measured galaxy redshifts at such extreme distances. In fact, for redshifts above 1 there are typically not enough measured galaxy redshifts to use TS methods with any accuracy, hence SED fitting has been used exclusively for z>1. See Benítez (2000) for an excellent detailed discussion of the differences and similarities between these two commonly used approaches.

In the past 10 years a large number of empirical fitting techniques for TS methods have come into use and new techniques continue to be developed. Some examples of linear and non-linear methods include: 2nd and 3rd order polynomial fitting (Brunner et al. 1997); quadratic polynomial fitting (Connolly et al. 1995; Hsieh et al. 2005); Support Vector Machines (Wadadekar 2005); and the Artificial Neural Network method of Collister & Lahav (2004).

We explore the problem of estimating redshifts from broad-band photometric measurements using the idea of a Virtual Sensor (Srivastava 2005; Srivastava & Stroeve 2003). These methods allow for the estimation of unmeasured spectral phenomena based on learning the potentially nonlinear correlations between observed sets of spectral measurements. In the case of estimating redshifts, we can learn the nonlinear correlation between spectroscopically measured redshifts and broad-band colors. Statistically speaking, this amounts to building a regression model to estimate the photometric redshift. However, the procedure is much more complex than a simple regression due to the significant effort required for model building and validation. The concept of Virtual Sensors applies to the entire chain of analytical steps leading up to the prediction of the redshift. Figure 1 shows a schematic of the assumptions behind a Virtual Sensor with a cartoon on the left and the real-world case with the five SDSS bandpasses and a sample galaxy spectrum overlayed on the right.

As a baseline comparison, results from a TS based Neural Network package called ANNz (Collister & Lahav 2004) are presented. Linear and quadratic fits along the lines discussed in Connolly et al. (1995) are also presented. Unlike all other previous work, we also discuss the application of bootstrap resampling (Efron 1979; Efron & Tibshirani 1993) for the linear,

quadratic, and ANNz models.

We apply the TS methods discussed above to the SDSS five color (ugriz) imaging survey known as the Main Galaxy Sample (MGS, Strauss et al. 2002) which has a large calibration set of spectroscopic redshifts for the SDSS Data Release 2 (DR2, Abazajian et al. 2004) and SDSS Data Release 3 (DR3, Abazajian et al. 2005). The Two Micron All Sky Survey[2] extended source catalog along with Galaxy Evolution Explorer (GALEX, Martin et al. 2005)[3] data are also used in conjunction with the SDSS where all three overlap to create a combined catalog for use with our TS methods.

The datasets used in our analysis are discussed in § 2, discussion of the photometry and spectroscopic quality of the datasets along with other photometric pipeline output properties of interest in § 3, the classification schemes used to obtain photometric redshifts in § 4, comparison of the results in § 5, and we summarize in § 6.

2. The Sloan Digital Sky Survey, The Two Micron All Sky Survey and The Galaxy Evolution Explorer Datasets

Most of the work herein is related to the SDSS MGS DR2 and DR3, and the photometric quantities associated with them. For completeness we have added the 2MASS extended source catalog and GALEX All Sky Survey photometric attributes where data exists for the same SDSS MGS galaxies with corresponding redshifts. The 2MASS and GALEX data samples are small where they overlap with those of the SDSS MGS galaxies with corresponding known spectroscopic redshifts in the DR2 and DR3. However, they appear copious enough for our new TS methods as there is no evidence of over-fitting of these smaller data samples.

The Sloan Digital Sky Survey (York et al. 2000) will eventually encompass roughly 1/4 of the entire sky collecting five band photometric data in 7700 $\deg^2$ down to 23rd magnitude in r on of order 10^8 celestial objects. For about 1 in every 100 of these objects down to g∼20 a spectrum will be measured coming to a total of about 10^6 galaxy and quasar redshifts over roughly the same area of the sky (7000 $\deg^2$) as the photometric survey (Stoughton et al. 2002). The five broad-band filters used, u,g,r,i and z, cover the optical range of the spectrum (Table 1).

We use several catalogs derived from the SDSS. The MGS (Strauss et al. 2002) of the

---

[2]http://www.ipac.caltech.edu/2mass/

[3]http://www.galex.caltech.edu/

SDSS is a magnitude limited survey that targets all galaxies down to $r_{Petrosian}<17.77$. We use the MGS from DR2 and DR3 where spectroscopic redshifts exist in order to validate our methods.

The 2MASS extended source catalog contains positions and magnitudes in j, h, and k_s filters for 1,647,599 galaxies and other nebulae across the entire sky (Table 1). The extended source magnitude limits in the 3 filters are j=15.0, h=14.3 and k_s=13.5. See Jarrett et al. (2000) for more detailed information on the extended source catalog.

The GALEX data release 1 (GR1)[4] All-Sky photometry catalog contains positions and magnitudes in two Ultraviolet bands called the Far Ultraviolet Band (FUV) and the Near Ultraviolet Band (NUV). See Table 1 for details on these broad-band pass filters. Limiting magnitudes for the All-Sky (100 second integrations) FUV is 19.9 and 20.8 for the NUV. See Morrissey et al. (2005) and references therein for more details of the in-orbit instrument performance and Martin et al. (2005) for mission details. The All-Sky GR1 covers 2792 deg^2 of the sky.

3. Photometric and redshift quality, morphological indicators and other catalog properties

Historically most determinations of photometric redshifts from large photometric surveys contain only broad-band magnitudes without reference to other parameters that may have been available from the photometric aperture reductions themselves. With the SDSS most papers have utilized only the five band photometry (ugriz) while a host of additional parameters like Petrosian radii (Strauss et al. 2002), measures of ellipticity (Stoughton et al. 2002), and other derived quantities are readily available from the photometric pipeline reductions.

This section explains the various quality flags used to obtain data from the SDSS photometric and redshift catalogs, the photometric catalogs of the 2MASS extended source catalog and the GALEX All Sky survey. We also explore the most likely candidates to yield information related to the prediction of redshifts in the Main Galaxy Sample (MGS) of the SDSS for our TS calculations. The last subsection (§ 3.6) describes the four dataset types used in our analysis.

---

[4]http://galex.stsci.edu/GR1/

3.1. The SDSS photometric quality flags

The SDSS photometric pipeline (Lupton et al. 2001) produces a host of quality flags (Stoughton et al. 2002, Table 9) giving additional information on how the photometry was estimated. The primtarget flag is used to make sure the Main Galaxy Sample is chosen and extinction corrected model magnitudes (Stoughton et al. 2002) are used throughout this work (See query in Appendix I).

Herein we define GOOD and GREAT quality photometry (see Table 2 for a description) where ! means NOT:

GOOD: !BRIGHT and !BLENDED and !SATURATED

GREAT: GOOD and !CHILD and !COSMICRAY and !INTERP

In this manner one can determine if a difference in the quality of the photometry makes any difference in the errors of the estimated photometric redshifts. The only reason not to always use the very best photometry (what we call GREAT in this work) is that the total number of galaxies can drop by orders of magnitude and hence one may end up sampling a much smaller number of objects. However, not everyones needs are the same and hence the quality can be weighted based on what is desirable. See Appendix I for the complete SDSS skyserver[5] queries used to obtain the data used in this paper.

3.2. The SDSS redshift quality flags

The SDSS spectroscopic survey (Stoughton et al. 2002; Newman et al. 2004) has several flags to warn the user of poor quality redshifts that come from the spectroscopic pipeline reductions (Stoughton et al. 2002). This is important because an inaccurate training-set will result in poor results no matter which method is used. To this end we utilized an estimate of the confidence of the spectroscopic redshift called zConf. Hence only those galaxies with zConf>0.95 in the MGS are chosen. Other authors (e.g. Wadadekar 2005) have chosen to use only the zWarning flag set to zero. Our studies find zConf values far below that of 0.95 when only the zWarning=0 flag is set. This may put into question the reliability of such redshift estimates. In addition, by setting zConf to values greater than 0.95, as we have done, the zWarning=0 flag is also included.

––––––––––––––––––––––––––––––––––

[5]http://casjobs.sdss.org

Table 1: Survey filters and characteristics

Bandpass	Survey	λ_{eff} (Å)	$\Delta\lambda$ (Å)	FWHM [1] ($''$)
FUV	GALEX	1528	442	4.5
NUV	GALEX	2271	1060	6.0
u	SDSS	3551	600	1-2
g	SDSS	4686	1400	1-2
r	SDSS	6165	1400	1-2
i	SDSS	7481	1500	1-2
z	SDSS	8931	1200	1-2
j	2MASS	12500	1620	2-3
h	2MASS	16500	2510	2-3
k_s	2MASS	21700	2620	2-3

[1] Dependent upon seeing at time of observation for ground based data.

Table 2: Photometric Quality Flags used in this paper [a]

Name	Bitmask	Description
BRIGHT	0x00002	Object detected in first bright object finding step; generally brighter than r=17.5
BLENDED	0x00008	Object had multiple peaks detected within it
SATURATED	0x40000	Object contains one or more saturated pixels
CHILD	0x00010	Object product of attempt to deblend BLENDED object
COSMICRAY	0x01000	Contains pixel interpreted to be part of a cosmic ray
INTERP	0x20000	Object contains pixel(s) values determined by interpolation

[a] Stoughton et al. (2002)

3.3.   2MASS photometric quality and cross-reference with the SDSS

Given the high quality constraints of the published photometry of the 2MASS extended source public release catalog (Jarrett et al. 2000), only one quality flag is checked. The extended source catalog confusion flag, "cc_flg", is required to be zero in all three band passes.

The j_m_k20fe, h_m_k20fe, and k_m_k20fe isophotal fiducial elliptical aperture magnitudes as defined in the 2MASS database are extracted for the respectively described j, h, and k_s 2MASS magnitudes used in this work.

The extended source catalog was loaded into our local SQL database containing the SDSS DR2 to create a combined catalog (see next section).

3.4.   GALEX photometric quality and cross-reference with the SDSS

Near-Ultraviolet (nuv) and far-Ultraviolet (fuv) broad-band photometry are extracted from the GALEX database for our use. Several quality flags are used to make sure the data are of the highest quality. Bad photometry values in nuv photometry (nuv_mag) and fuv photometry (fuv_mag) are given the value of -99 in the GR1 database and these are excluded from our catalog if either or both filters contain such a value. The nuv_artifact=0 flag is set to avoid all objects with known bad photometry artifacts. Hence if nuv_artifact has any value other than zero the nuv_mag is considered bad. Currently fuv_artifact is always zero in the GR1. The band=3 flag is used since it indicates detection in both nuv and fuv bands. Finally, a value of fov_radius<0.55 is required as this is the minimum recommended value to make sure the distance of the object in degrees from the center of the field of view of the telescope is not too large, as this is known to cause problems in the quality of the photometry obtained.

As with the 2MASS extended source catalog, the GALEX All Sky data was loaded into our local SQL database now containing the SDSS DR2 and 2MASS catalogs. The SDSS MGS with redshifts and the 2MASS extended source catalogs were cross-referenced with GALEX when all three catalog positions agreed to within 5″. The methods and results used are comparable to those of Seibert et al. (2005) hence we do not go further into a description of the combined catalog. See Appendix I for a sample query.

3.5. SDSS Petrosian Radii, Inverse Concentration Index, FracDev, and Stokes

The photometry properties discussed below are available in all five SDSS bandpasses (ugriz), but we use the r bandpass values for these quantities as, in general, the r band result has the lowest error and gives more consistent results. This is also reasonable given the low redshifts used, but this strategy would be questionable at higher redshifts when morphological features in the rest frame r band start to get more strongly shifted to the i and z bands.

It has been shown that using Petrosian (1976) 50% and 90% flux radii (Wadadekar 2005) in addition to the SDSS five band photometry one can improve results by as much as 15% (see Table 3). The Petrosian 50% (90%) radius is the radius where 50% (90%) of the flux of the object is contained. Given the low redshifts of this catalog they can be assumed to be a rough measure of the angular size of the object. The ratio of these quantities is called the Petrosian inverse concentration index (CI) $1/c \equiv r_{50}/r_{90}$ which measures the slope of the light profile. The concentration index corresponds nicely to eyeball morphological classifications of large nearby galaxies (Strateva 2001; Shimasaku et al. 2001).

The Petrosian Radii are also used in combination with a measure of the profile type from the SDSS photometric pipeline reduction called FracDev. FracDev comes from a linear combination of the best exponential and de Vaucouleurs profiles which are fit to the image in each band. FracDev is the de Vaucouleurs term (§3.1, Abazajian et al. 2004). It is one for a pure de Vaucouleurs profile typical of early type galaxies and zero for a pure exponential profile typical of late type galaxies. FracDev is represented as a floating point number between zero and one. This is similar to the use of the Sérsic n-index (Sérsic 1968) for morphological classification. The idea of using FracDev as a proxy for the Sérsic index n comes from Vincent & Ryden (2004) who show that if Sérsic profiles with 1<n<4 accurately describe the SDSS galaxy early and late types then FracDev is a "monotonically increasing function of the Sérsic index n, and thus can be used as a surrogate for n". For a recent discussion on Sérsic profiles see Graham & Driver (2005). Blanton et al. (2003a,b) have also shown that Sérsic fits to the azimuthally averaged radial profile of an SDSS object provide a better estimate of galaxy morphology than the Petrosian inverse concentration index ($1/c \equiv r_{50}/r_{90}$) for the majority of MGS objects. However, at the time of this work these profiles were only available in the derived SDSS DR2 NYU-VAGC catalog of Blanton et al. (2005) and our own studies do not show appreciable improvement over the Petrosian inverse concentration index when used to calculate photometric redshifts.

Measures of galaxy ellipticity and orientation, as projected on the sky, can be obtained from the SDSS photometric pipeline "Stokes" parameters Q and U (Stoughton et al. 2002).

These are the flux-weighted second moments of a particular isophote.

$$M_{xx} \equiv \langle \frac{x^2}{r^2} \rangle, \quad M_{yy} \equiv \langle \frac{y^2}{r^2} \rangle, \quad M_{xy} \equiv \langle \frac{xy}{r^2} \rangle \tag{1}$$

According to Stoughton et al. (2002) when the isophotes are self-similar ellipses one finds

$$Q \equiv M_{xx} - M_{yy} = \frac{a-b}{a+b}\cos(2\phi), \quad U \equiv M_{xy} = \frac{a-b}{a+b}\sin(2\phi), \tag{2}$$

Since the Stokes values are related to the axis ratio and position angle, using these quantities in combination with those above should give additional information on the galaxy types we are sampling and hence help in the estimation of photometric redshifts. However, in our studies we only utilize the Q parameter defined above as we see no improvement when using both Q and U.

3.6. Description of the four dataset types used

Four classes of datasets are used in our analysis, based on the descriptions above.

Dataset 1: SDSS MGS GOOD quality photometry. All of the data comes from the SDSS MGS with the GOOD quality flags set. There are 6 subsets in this dataset as seen in the left hand side of Figure 3.

1. u-g-r-i-z: contains only the SDSS five band extinction corrected magnitudes.

2. u-g-r-i-z-petro50-petro90: contains the u-g-r-i-z data and the Petrosian 50% and 90% radii in the r band.

3. u-g-r-i-z-petro50-petro90-ci: contains the u-g-r-i-z-petro50-petro90 data and the Petrosian concentration index as described in § 3.5.

4. u-g-r-i-z-petro50-petro90-ci-qr: contains the u-g-r-i-z-petro50-petro90-ci and the Stokes Q parameter as described in § 3.5.

5. u-g-r-i-z-petro50-petro90-fracdev: contains the u-g-r-i-z-petro50-petro90 and the FracDev parameter as described in § 3.5.

6. u-g-r-i-z-petro50-petro90-qr-fracdev: contains the u-g-r-i-z-petro50-petro90-fracdev and the Stokes Q parameter as described in § 3.5.

The total dataset consists of 202,297 galaxies.

Dataset 2: SDSS MGS GREAT quality photometry. All of the data, as seen in Figure 4, comes from the SDSS MGS with the GREAT quality flags set. There are 6 subsets named and described in the same way as for Dataset 1. The total dataset consists of 33,328 galaxies.

Dataset 3: GALEX GR1, SDSS MGS GOOD quality photometry, and the 2MASS extended source catalogs labeled as nuv-fuv-ugriz-jhk. As seen in the left hand side of Figure 5, it consists of the two Ultraviolet magnitudes from the GALEX GR1 database (nuv and fuv). It has the five SDSS MGS extinction corrected magnitudes (u,g,r,i,z) with the GOOD quality photometry flags set, but unlike Datasets 1 and 2 there are no other SDSS inputs used. It also contains the three 2MASS extended source catalog magnitudes (j,h,k_s). The total dataset consists of 3095 galaxies.

Dataset 4: GALEX GR1, SDSS MGS GREAT quality photometry, and the 2MASS extended source catalogs. As shown on the right hand side of Figure 5 it is nearly the same as Dataset 3, except the SDSS MGS GREAT quality photometry flags are set. The total dataset consists of 326 galaxies.

4.   Training Methods

We estimate the photometric redshifts of the galaxies in the SDSS, 2MASS and GALEX databases using several classes of algorithms: simple linear and quadratic regression, neural networks and Gaussian processes. These methods have different properties and make different assumptions about the underlying data generating process which will be discussed below.

4.1.   Linear and Quadratic fits

Linear and quadratic polynomial fitting along the lines of Connolly et al. (1995); Hsieh et al. (2005) are used as a way to benchmark the new methods discussed below. The linear regression for the SDSS ugriz magnitudes would be given by an equation of the form:

$$Z = A + Bu + Cg + Dr + Ei + Fz \tag{3}$$

Where A, B, C, D, E, and F result from the fit. All data points are weighted equally. Z is the photometric redshift.
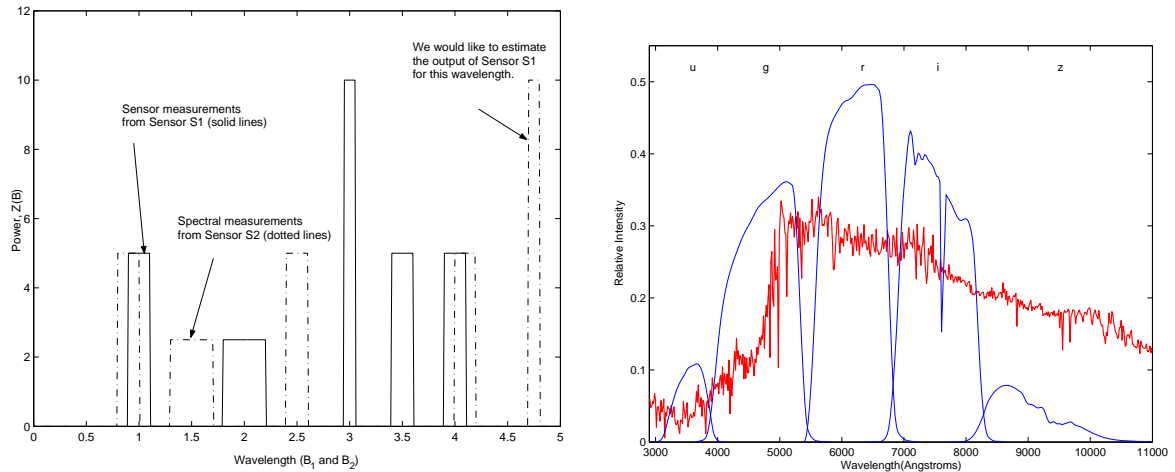
Fig. 1.— The left figure is a cartoon to help illustrate the need for a Virtual Sensor. We have spectral measurements from two sensors $\mathcal{S}_1$ and $\mathcal{S}_2$, (solid and dot-dashed lines, respectively). We wish to estimate the output of sensor $\mathcal{S}_1$ for a wavelength where there is no actual measurement from the sensor. Note that some sensor measurements overlap perfectly, as in the case of wavelength = 3, and in other cases, such as wavelength = 1, there is some overlap in the measurements. The right figure shows the sensitivity through an airmass of 1.3 for extended sources in the five SDSS (u,g,r,i,z) filter bandpasses with the spectrum of NGC5102 (Storchi-Bergmann et al. 1995) purposely redshifted 1000Å overlayed.

The quadratic form is similar and again all points are weighted equally.

$$Z = A + Bu + Cg + Dr + Ei + Fz + Guu + Hgg + Irr + Jii + Kzz + Lug + Mur + Nui + Ouz + Pgr + Qgi + Rgz + Sri + Trz + Uiz \quad (4)$$

4.2. The Artificial Neural Networks approach

The Artificial Neural Network (ANNz) approach of Collister & Lahav (2004) is specifically designed to calculate photometric redshifts from any galaxy properties the user deems desirable. It has been demonstrated to work remarkably well on the SDSS DR1 (Collister & Lahav 2004). The ANNz package contains code to run back-propagation neural networks with arbitrary numbers of hidden units, layers and transfer functions. We chose 2 hidden units, and 10 nodes in each of these units (see Figure 2). See the next section for a more detailed description of neural networks in general, or see Collister & Lahav (2004).

4.3.   The Ensemble Model

Back-propagation neural networks have been used extensively in a variety of applications since their inception. A good summary of the methods we use can be found in Bishop (1995). Neural networks are a form of nonlinear regression in which a mapping, defined as a linear combination of nonlinear functions of the inputs, are used to approximate a desired target value. The weights of the linear combination are usually set using an approach, based on gradient descent of a cost function, that is defined between the target value and the estimated value. The cost function usually has multiple local minima, and the model obtained at the end of a training cycle usually corresponds to one such minima and not to a global minimum. The global minimum would correspond to the model that best approximates the training set. Generalization of the model on a test set (i.e., data that is not used during the model building phase) can be shown to be poor if a global minimum is reached due to the phenomenon of over-fitting.

The following material is a standard demonstration that although the neural network computes a nonlinear function of the inputs, distribution of errors follows a Gaussian if the squared error cost function is minimized. The cost function encodes an underlying model of the distribution of errors. For example, suppose we are given a data set of inputs $\mathcal{X}$, targets $\mathcal{Y}$, and a model parameterized by Θ. The standard method of obtaining the parameter Θ is by maximizing the likelihood of observing the data $\mathcal{D} = (\mathcal{X}, \mathcal{Y})$ with the model Θ. Thus, we need to maximize:

$$
\begin{aligned}
P(\Theta|\mathcal{D}) &= \frac{P(\mathcal{D}|\Theta)P(\Theta)}{P(\mathcal{D})} \\
&\propto P(\mathcal{D}|\Theta)P(\Theta)
\end{aligned}
$$

and we note that $P(\mathcal{D}|\Theta) = P(\mathcal{X}, \mathcal{Y}|\Theta)$ and so:

$$
P(\mathcal{X}, \mathcal{Y}|\Theta) = P(\mathcal{Y}|\mathcal{X}, \Theta)P(\mathcal{X}|\Theta) \tag{5}
$$

The function $P(\Theta)$ represents the prior distribution over model parameters. If we have knowledge about the ways in which the weights of the model are distributed *before the data arrives*, such information can be encoded in the prior. Neal (1996) has shown that in the limit of an infinitely large network, certain simple assumptions on the distribution of the initial weights make a neural network converge to a Gaussian process. If we assume that the errors are normally distributed, we can write the likelihood of an input pattern $\mathbf{x}_i \in \mathcal{X}$

having target $y_i \in \mathcal{Y}$ with variance σ^2 as [6]:

$$
\begin{aligned}
L(y_i|\mathbf{x}_i, \Theta) & = P(y_i|\mathbf{x}_i, \Theta) \\
& = \frac{1}{\sqrt{2\pi}\sigma} \exp -\frac{(y_i - \hat{y}_i)^2}{2\sigma^2}
\end{aligned}
$$

The product of these likelihoods across the N data points in the data set $\mathcal{D}$ is the likelihood of the entire data set:

$$
\begin{aligned}
P(\mathcal{Y}|\mathcal{X}, \Theta) & = \prod_{i=1}^{N} P(y_i|\mathbf{x}_i, \Theta) \\
& = \prod_{i=1}^{N} \frac{1}{\sqrt{2\pi}\sigma} \exp -\frac{(y_i - \hat{y}_i)^2}{2\sigma^2}
\end{aligned}
\tag{6}
$$

¿From this equation, it is straightforward to see that maximizing the log of this likelihood function is equivalent to minimizing the squared error, which is the standard cost function for feed-forward neural networks used in regression problems.

Neural networks are often depicted as a directed graph consisting of nodes and arcs as shown in Figure 2. For a p dimensional input $\mathbf{x}$ the value at the k hidden nodes $\mathbf{z}$ is the $k \times 1$ vector:

$$
\mathbf{z} = s(W_1\mathbf{x} + \mathbf{b}_1)
\tag{7}
$$

and the final estimate of the target y is given by $\hat{y}$:

$$
\begin{aligned}
\hat{y} & = W_2\mathbf{z} + \mathbf{b}_2 \\
& = f(\mathbf{x}, \Theta)
\end{aligned}
\tag{8}
$$

where W_1 is a $k \times p$ matrix, $\mathbf{b}_1$ is a $p \times 1$ vector, W_2 is a $k \times l$ matrix and $\mathbf{b}_2$ is an $l \times 1$ vector. In the case where the network only generates one output per input pattern as is the case in the studies presented here, $l = 1$.

The function s is a nonlinear function and is chosen as a sigmoid:

$$
s(a) \equiv \frac{1}{1 + exp(-a)}.
\tag{9}
$$

Neural networks are trained to fit data by maximizing the likelihood of the data given the parameters. The model obtained through this maximization process corresponds to a

---

[6]We follow the convention that bold-faced notation indicates vectors and non-bold faced symbols indicate scalars
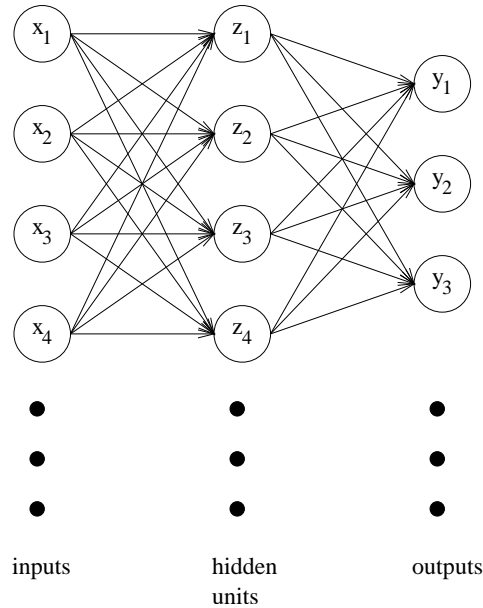
Fig. 2.— A graphical depiction of a neural network with 4 inputs, 4 hidden units, and 3 outputs. The outputs are nonlinear functions of the inputs.

single model sampled from the space of models parameterized by the model parameters Θ. If we assume Gaussian errors, we have shown that the cost function is the well-known sum-squared error criterion. The network is trained by performing gradient descent in the parameter space Θ. The derivative of this cost function with respect to each weight in the network is calculated and the weights are adjusted to reduce the error. Because the cost function is non-convex, the optimization problem gets caught in local minima, thus making training and model optimization difficult. In order to reduce the effects of local minima, we performed *bagging* or Bootstrap AGgregation (Breiman 1996). In this procedure, we sample the data set $\mathcal{D}$ M times with replacement. For each sample, we build one neural network in the ensemble of M neural networks. The final prediction is formed by taking the mean prediction of all M neural networks:

$$\hat{y} = \frac{1}{M} \sum_{i=1}^{M} \hat{y}_i \tag{10}$$

Breiman (1996) showed that this procedure results in a regression model with lower error. Our results, which we term our "Ensemble Model" (see Tables 4–6), show the effects of the local minima and the distribution of errors that result from this problem on the SDSS, 2MASS and GALEX data sets.

4.4.   Kernel Methods and Gaussian Processes

In many ways, neural networks are attractive models for nonlinear regression problems because they can scale to large data sets, and provide a good baseline from which to compare other methods. In the machine learning literature, kernel methods have in many ways subsumed neural networks because it was shown that as the number of hidden units increases, if we assume that the weights and biases of the neural network are drawn from a Gaussian distribution (thus assuming that $P(\Theta)$ is Gaussian), the prior distribution over functions implied by such weights and biases converges to a Gaussian process (Neal 1996; Cristianini & Shawe-Taylor 2000).

To describe a Gaussian process, we first note that in the case of a neural network, $\hat{y}$ is defined as a specific nonlinear function of $\mathbf{x}$, parametrized by Θ, $\hat{y} = f(\mathbf{x}, \Theta)$. In a Gaussian process, we actually define a prior distribution over the space of functions f which is assumed to be Gaussian. Thus, we have:

$$P[(f(\mathbf{x}_1), f(\mathbf{x}_2), ..., f(\mathbf{x}_N)) = (y_1, y_2, ..., y_N)] \propto \exp(-\frac{1}{2}\mathbf{y}^T\Sigma^{-1}\mathbf{y}). \tag{11}$$

The marginals for all subsets of variables of a Gaussian process are Gaussian. The covariance matrix Σ measures the degree of correlation between inputs $\mathbf{x}_i$ and $\mathbf{x}_j$. The choice of the correlation function Σ defines a potentially nonlinear relationship between the inputs and the outputs. If we choose $\Sigma(\mathbf{x}_i, \mathbf{x}_j) = K(\mathbf{x}_i, \mathbf{x}_j)$, where K is a positive definite function, we obtain a specific Gaussian process induced by the kernel function K. To make a prediction with a Gaussian process, we assume that a covariance function has been chosen, and then compute:

$$P(y_{N+1}) = \frac{P(y_{N+1}, \mathbf{y})}{P(\mathbf{y})} \tag{12}$$

We know that this distribution will be Gaussian, and the mean and variance of the distribution can be computed as follows Cristianini & Shawe-Taylor (2000):

$$\hat{y}_{N+1} = f(\mathbf{x}_{N+1}) \;\; = \;\; \mathbf{y}^T(K + \lambda^2 I)\mathbf{k} \tag{13}$$

$$\sigma^2(\mathbf{x}_{N+1}) \;\; = \;\; \Sigma(\mathbf{x}_{N+1}, \mathbf{x}_{N+1}) - \mathbf{k}^T(K + \lambda^2 I)^{-1}\mathbf{k} \tag{14}$$

where $\mathbf{k} = \Sigma(\mathbf{x}_i, \mathbf{x})$, $K = K(\mathbf{x}_i, \mathbf{x}_j)$ and λ is an externally tuned parameter that represents the noise in the output.

The nonlinearity in the model comes from the choice of the kernel function K. Typical choices for K include the radial basis function: $K(\mathbf{x}_i, \mathbf{x}_j) = \exp(-\frac{1}{2\sigma^2}||\mathbf{x}_i - \mathbf{x}_j||^2)$ or the polynomial kernel $K(\mathbf{x}_i, \mathbf{x}_j) = (1 + \mathbf{x}_i^T\mathbf{x}_j)^r$. We choose the latter for this study.
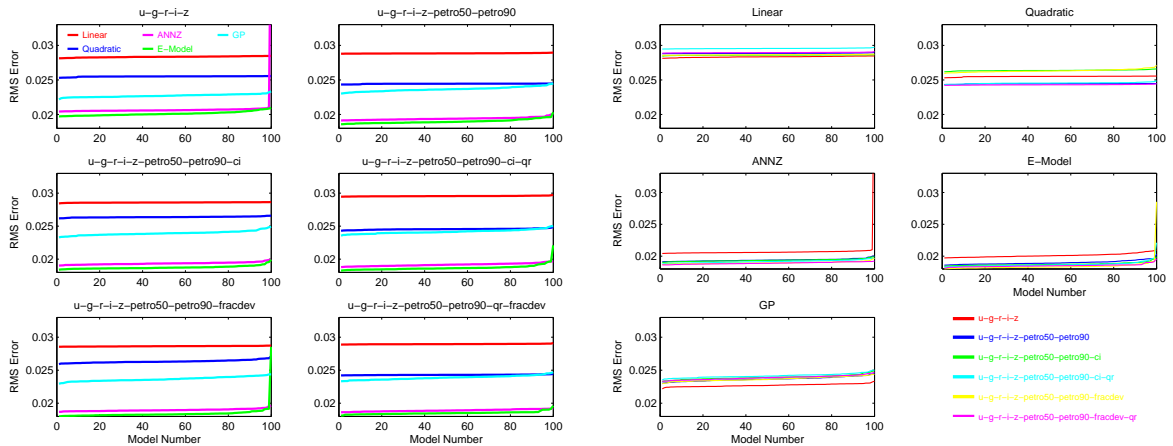
Fig. 3.— The six plots to the left contain the five training methods for each of the six inputs applied to the SDSS GOOD datasets known as Dataset 1. The five plots to the right are our training-set results for each of the five training methods applied to the six different SDSS GOOD inputs.

It can be shown that Gaussian process regression, as described above, builds a linear model in a very high dimensional feature space which is induced by the nonlinear kernel function K. One distinct advantage of the Gaussian process is that it delivers point predictions as well as a confidence interval around the predictions.

5. Discussion

Results discussed below include the two different SDSS photometric quality flag combinations used called GOOD and GREAT. For the SDSS data 10 different photometric pipeline output parameters are utilized in different combinations (see § 3.6): u,g,r,i, and z extinction corrected model magnitudes, r band Petrosian 50% flux radii (petro50) and Petrosian 90% flux radii (petro90), the Petrosian inverse concentration index (CI) derived from these two quantities, the r band FracDev quantity (FD), and r band Stokes value all as defined in § 3.5 and 3.6. Results are also discussed from the combined catalogs of the SDSS MGS (u,g,r,i,z magnitudes only) galaxies with redshifts, the 2MASS extended source catalog (j,h,k$_s$ magnitudes), and GALEX All-Sky (nuv,fuv magnitudes) data sets. The sample sizes for each of these datasets are also given in Tables 4–6.

In order to make our results as comparable as possible the same validation, training and testing sizes are used in our analysis for ANNz, Ensemble Model, linear and quadratic fits: training=89%, validation=1% and testing=10%. In order to put proper confidence intervals on the error estimates from these methods bootstrap resampling (Efron 1979; Efron
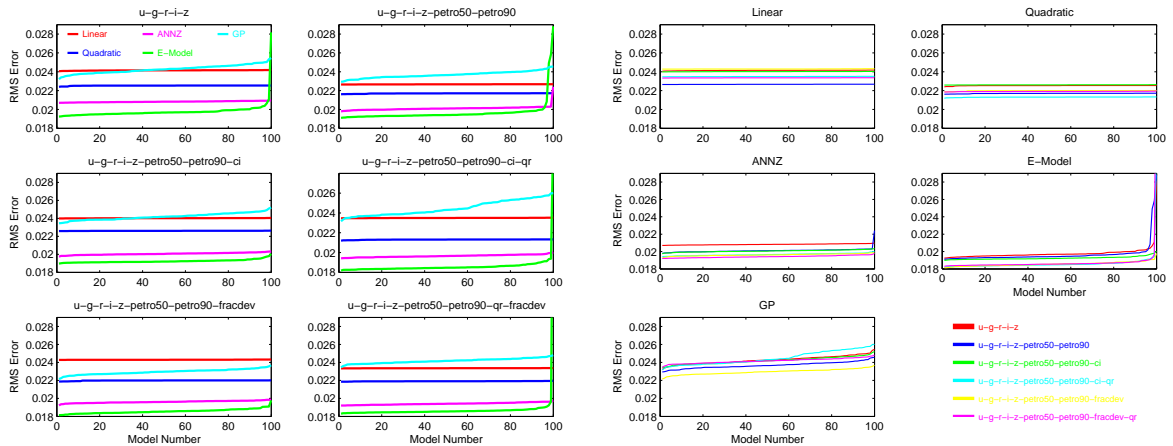
Fig. 4.— The six plots to the left contain the five training methods for each of the six inputs applied to the SDSS GREAT datasets known as Dataset 2. The five plots to the right are our training-set results for each of the five training methods applied to the six different SDSS GREAT inputs.

& Tibshirani 1993) is utilized on the training data. 90% of the training data is used for each of 100 bootstraps.

For the Gaussian processes the situation is slightly different. The same percentages for training, validation, and testing are utilized. However, for Datasets 1-3 1000 samples from the training data are used for each of the bootstrap runs. For Dataset 4 only 50 samples are utilized for each of the bootstrap runs. The Gaussian processes require matrix inversion which is an $O(N^3)$ operation. Hence small training sets were required to complete this project in a reasonable time frame.

In Tables 4–6 we report robust 90% confidence intervals around our 50% RMS result for all of these methods from the bootstrap resampling. Figures 3, 4 and 5 show the same information, albeit in a more detailed graphical format.

Table 4 and Figure 3 demonstrate our results on Dataset 1. The plots in Figure 3 clearly demonstrate that the ANNz and E-Model neural network methods are superior in their accuracy over nearly all bootstrap samples (labeled "model number" in Figures 3-5) no matter which input quantities are used. The linear and quadratic fits fair the worse as is expected. The Gaussian process model is usually found in between. However, it must be remembered that only ∼1000 sample points are used for training in each case and therefore it is possible that it is not sampling all of the possible redshift-color space. Nonetheless it does an excellent job given the small data samples used in comparison to the other methods. It is also clear that the inputs used reproduce very similar results once one goes beyond the five band magnitudes of the SDSS and quantities like the Petrosian concentration index or

the Stokes measure of ellipticity are used. The best method, our Ensemble Model, regularly reproduces RMS values of less than 0.019 no matter the confidence level (or bootstrap sample) used.

Table 5 and Figure 4 for Dataset 2 give very similar results to that of Dataset 1 just discussed. Lower RMS errors are obtained than that of the GOOD quality data, but there is more variation in the confidence intervals evidenced by increasing slope as a function of bootstrap sample in Figure 4. As with Dataset 1, the RMS error results are lower but similar when the five band SDSS magnitudes are supplemented with quantities like the Petrosian radii, or the FracDev measurement.

While Dataset 2 does on occasion have slightly better RMS errors than Dataset 1 in general there is little difference in the use of higher quality photometry and we would not recommend the use of the higher quality photometry of Dataset 2 as described herein in general.

Table 6 and Figure 5 are the results of using Datasets 3 and 4. The right hand side of Figure 5 for Dataset 4 (which has better photometric quality) shows again an increase in the variability of the RMS error as a function of bootstrap sample larger than that of the GOOD sample from Dataset 3 to the left. In general the right hand side plot with the better SDSS photometry of Dataset 4 has RMS errors either the same or worse than those from the SDSS only Datasets 1 and 2 in Figures 3 and 4. The variability in the RMS error as a function of bootstrap and the generally large RMS errors leads one to believe that the sample size is too small to train on. Given that there are only 326 objects in Dataset 4 it shouldn't be too surprising. The apparent ability of the quadratic regression to do so well might point one to possible over-fitting of the data.

However, on the left hand side of Figure 5 the story for Dataset 3 is very different. Here the variability is much less as a function of bootstrap, the RMS errors are generally quite low and the prediction abilities of the different methods are consistent with those observed in the SDSS Datasets 1 and 2 found in Figures 3 and 4. The Ensemble Model once again surpasses all other methods for 95% of the bootstrap samples followed closely by the Gaussian processes and ANNz methods. Here one can see that the Gaussian process method is more competitive as it is likely to be sampling all possible templates of the 3095 input galaxies even with only 1000 samples per run.

In order to show the effects of sampling and local minima for the Ensemble Model on the quality of redshift predictions we show a set of 100 neural networks and show their final RMS errors in Figures 6 and 7. Each neural network is built by drawing a sample from the training set with replacement and then performing the gradient descent maximization process

described earlier. We train until the model converges, which is defined as the gradient-descent iteration at which the magnitude of the gradient drops below a preset threshold. This model corresponds to one point on the top panel of Figures 6 and 7.

The middle panel of Figure 7 shows the cumulative distribution function for the errors shown in the upper panel. The x-axis is the RMS error (e_0), and the y-axis is P(RMS $< e_0$). The plot indicates that about 70% of the models we generated have an RMS error less than 0.1. This plot also indicates that reporting the minimum observed RMS value, which is done throughout the literature on this topic (Collister & Lahav 2004, e.g. ANNz) is misleading. For the models computed for this empirical cumulative distribution function, the quantity P(RMS $< e_0$) rapidly vanishes as $e_0 \rightarrow 0.04$. This implies that such models are not only highly unlikely, but also highly non-robust.

In order to contrast this distribution with the empirical distributions observed on other data sets, we chose to show Figure 6. This figure, unlike the previous figure discussed, shows that the variation imposed by the optimization procedure, combined with the variations in the data set, have a relatively small effect on the quality of predictions: nearly 70% of the models have a very low error rate, with the distribution rapidly increasing after that. Notice that the empirical cumulative distribution function shown in the lower panel rises sharply at the onset of the curve. This indicates that 70% of the models have an error less than about 0.025. Again, this variation and apparent combined stability of the data set and optimization procedure would be entirely lost if only the minimum value of the distribution was reported.

For comparison in Figure 8 one can see the known spectroscopic redshift plotted against the calculated photometric redshift from the test data for our 5 algorithms used against the ugriz-petro50-petro90-ci-qr GREAT dataset (part of Dataset 2) as presented in Table 5. Notice that the Gaussian process plot (lower middle) has a larger number of points which is due to the smaller training set and larger testing sets used in this algorithm. The 6th plot in the lower right hand corner of Figure 8 contains the Gaussian process model results against the GREAT nuv-fuv-ugriz-jhk Dataset 4 as presented in Table 6.

6. Conclusion

We have shown that photometric redshift accuracy of SDSS photometric data can be improved over that of previous attempts through a careful choice of additional photometric pipeline outputs that are related to angular size and morphology. Adding additional bandpasses from the Ultraviolet (GALEX) and Infrared (2MASS) can be even more helpful, but the current sample sizes are presently too small to be useful for Large Scale Structure

studies.

We have also shown that there is little difference in the use of the higher quality SDSS photometry as defined herein. Hence we would not recommend its use because it decreases the sample size markedly and does not decrease the RMS errors in the photometric redshift prediction.

We wish to stress that when using a neural network model for studies of photometric redshifts care must be taken when reporting the results of such models. There is a tendency in the astronomical literature to report only the best fit model, which is often unlikely to be the one used to calculate the final photometric redshift estimates.

The effects of local minima on prediction has also been discussed in some detail and we describe the way in which an ensemble of neural networks can reduce the problem.

We have also discussed the result of using Gaussian processes for regression, which avoids many of the local minima problems that occur with neural networks. One of the great strengths of Gaussian processes as used herein is the ability to use small training sets, which may be helpful in high redshift studies where very small numbers of measured redshifts are available.

A.   SDSS Queries

Below are the queries used against the SDSS DR2 and DR3 databases to obtain the data used throughout this paper.

Query used to obtain Dataset 1:

```
Select p.ObjID, p.ra, p.dec,
p.dered_u, p.dered_g, p.dered_r, p.dered_i, p.dered_z,
p.petroR50_r, p.petroR90_r, p.fracDeV_r, p.q_r,
p.Err_u, p.Err_g, p.Err_r, p.Err_i, p.Err_z,
p.petroR50Err_r, p.petroR90Err_r, p.qErr_r,
s.z, s.zErr, s.zConf
into mydb.dr3cfracdpetq from SpecOBJall s, PhotoObjall p
WHERE s.specobjid=p.specobjid
and s.zConf>0.95
and (p.primtarget & 0x00000040 > 0)
and ( ((flags & 0x8) = 0) and ((flags & 0x2) = 0) and ((flags & 0x40000) = 0))
```

Query used to obtain Dataset 2:

```
Select p.ObjID, p.ra, p.dec,
p.dered_u, p.dered_g, p.dered_r, p.dered_i, p.dered_z,
p.petroR50_r, p.petroR90_r, p.fracDeV_r, p.q_r,
p.Err_u, p.Err_g, p.Err_r, p.Err_i, p.Err_z,
p.petroR50Err_r, p.petroR90Err_r, p.qErr_r,
s.z, s.zErr, s.zConf
```

into mydb.dr3cfracdpetq from SpecOBJall s, PhotoObjall p
WHERE s.specobjid=p.specobjid
and s.zConf>0.95
and (p.primtarget & 0x00000040 > 0)
and (((flags & 0x8) = 0) and ((flags & 0x2) = 0) and ((flags & 0x40000) = 0)
and ((flags & 0x10) =0) and ((flags & 0x1000)=0) and ((flags & 0x20000) = 0))

Query used to obtain Dataset 3:

Select p.objID, p.ra, p.dec,
g.NUV_MAG, g.NUV_MAGERR, g.FUV_MAG, g.FUV_MAGERR,
p.u, p.Err_u, p.g, p.Err_g, p.r, p.Err_r, p.i, p.Err_i, p.z, p.Err_z,
t.j_m_k20fe, t.j_msig_k20fe, t.h_m_k20fe, t.h_msig_k20fe, t.k_m_k20fe, t.k_msig_k20fe,
s.z, s.zErr, s.zConf
FROM TWOMASS.dbo.xsc t, BESTDR2.dbo.PhotoObjAll p, GALEXDRONE.dbo.nuvfuv
g, BESTDR2.dbo.SpecOBJall s
WHERE s.specobjid=p.specobjid
and s.zConf>0.95 and s.zWarning=0
and g.NUV_MAG>-99 and g.FUV_MAG>-99
and t.cc_flg='0'
and (p.primtarget & 0x00000040 > 0)
and ((flags & 0x8)=0) and ((flags & 0x2)=0) and ((flags & 0x40000)=0)
and p.objid=BESTDR2.dbo.fgetnearestobjideq(t.ra,t.dec,0.08333)
and p.objid=BESTDR2.dbo.fgetnearestobjideq(g.RA,g.DEC,0.08333)

Query used to obtain Dataset 4:

Select p.objID, p.ra, p.dec,
g.NUV_MAG, g.NUV_MAGERR, g.FUV_MAG, g.FUV_MAGERR,
p.u, p.Err_u, p.g, p.Err_g, p.r, p.Err_r, p.i, p.Err_i, p.z, p.Err_z,
t.j_m_k20fe, t.j_msig_k20fe, t.h_m_k20fe, t.h_msig_k20fe, t.k_m_k20fe, t.k_msig_k20fe,
s.z, s.zErr, s.zConf
FROM TWOMASS.dbo.xsc t, BESTDR2.dbo.PhotoObjAll p, GALEXDRONE.dbo.nuvfuv
g, BESTDR2.dbo.SpecOBJall s
WHERE s.specobjid=p.specobjid
and s.zConf>0.95 and s.zWarning=0
and g.NUV_MAG>-99 and g.FUV_MAG>-99

and t.cc_flg='0'
and (p.primtarget & 0x00000040 > 0)
and (((flags & 0x8)=0) and ((flags & 0x2)=0) and ((flags & 0x40000)=0)
and ((flags & 0x10) =0) and ((flags & 0x1000)=0) and ((flags & 0x20000) = 0))
and p.objid=BESTDR2.dbo.fgetnearestobjideq(t.ra,t.dec,0.08333)
and p.objid=BESTDR2.dbo.fgetnearestobjideq(g.RA,g.DEC,0.08333)

REFERENCES

Abazajian, K., et al. 2003, AJ, 126, 2081

Abazajian, K., et al. 2004, AJ, 128, 502

Abazajian, K., et al. 2005, AJ, 129, 1755

Babbedge, T.S.R., et al. 2004, MNRAS, 353, 654

Baum, W.A. 1962, IAUS, 15, 390

Benítez, N. 2000 ApJ, 536, 571

Bishop, C.M. 1995 *Neural networks for pattern recognition*, Oxford University Press, New
    York

Blake, C. & Bridle, S. 2005, MNRAS, 363, 1329

Blanton, M.R., et al. 2003, ApJ, 594, 186

Blanton, M.R., Eisenstein, D., Hogg, D.W., Schlegel, D.J., & Brinkmann, J. 2005, ApJ, 629,
    143

Blanton, M.R., et al 2005, AJ, 129, 2562

Breiman, L. 1996, *Bagging predictors*, Machine Learning, 24, no. 2, 123–140

Brunner, R.J., Connolly, A.J., Szalay, A.S., & Bershady, M.A. 1997, ApJ, 482, L21

Collister, A.A. & Lahav, O. 2004, PASP, 116, 345

Connolly A.J., Csabai, I., Szalay, A.S., Koo, D.C., Kron, R.G., & Munn, J.A. 1995, AJ, 110,
    2655

Cristianini, N. & Shawe-Taylor, J. 2000, *An introduction to support vector machines*, Cambridge University Press

Csabai, I., et al. 2003, AJ, 125, 580

Efron, B., 1979. Bootstrap methods: Another look at the jackknife. The Annals of Statistics, 7, 1-26

Efron, B., & Tibshirani, R.J. 1993, An introduction to the bootstrap. New York, Chapman & Hall

Graham, A.W., & Driver, S.P. 2005, PASA, 22, 118

Hsieh, B.C., Yee, H.K.C., Lin, H., & Gladders, M.D. 2005, ApJS, 158, 161

Jarrett, T.H., Chester, T., Cutri, R., Schneider, S., Skrutskie, M., & Huchra, J.P. 2000, AJ, 119, 2498

Kodama, T., Bell, E.F., & Bower, R.G. 1999, ASP Conf. Ser. 191, Photometric Redshifts and High Redshift Galaxies, ed. R.J. Weymann, L.J. Storrie-Lombardi, M. Sawicki, & R.J. Brunner, 160

Koo, D.C., 1985 AJ, 90, 418

Lupton, R.H., Gunn, J.E., Ivezić, Ž., Knapp, G.R., Kent, S., & Yasuda, N. 2001, ASP Conf Proc. 238, Astronomical Data Analysis Software and Systems X, ed. F.R. Harnden Jr., F.A. Primini, & H.E. Payne, 269

Neal R.M. 1996, *Bayesian learning for neural networks*, Springer-Verlag New York, Inc., Secaucus, NJ, USA

Lanzetta, K.M., Yahil, A., & Fernandez-Soto, A. 1996, Nature, 381, 759

Loh, E.D., & Spillar, E.J. 1986, ApJ303, 154

Martin, D. C., et al. 2005, ApJ, 619, L1

Morrissey, P., et al. 2005, ApJ, 619, L7

Newman, P., et al. 2004, SPIE, 5492, 533

Padmanabhan, N. et al. 2005, MNRAS, 359, 327

Petrosian, V. 1976, ApJ, 209, L1

Seibert, M., et al. 2005, ApJ, 619, L23

Sérsic, J.L. 1968, Atlas de Galaxias Australes (Cordoba: Obs. Astron.)

Shimasaku, K., et al. 2001, AJ, 122, 1238

Srivastava, A.N., & Stroeve, J. 2003, *Onboard detection of snow, ice, clouds, and other geophysical processes using kernel methods*, Proceedings of the ICML 2003 Workshop on Machine Learning Technologies for Autonomous Space Applications

Srivastava, A.N., Oza, N.C. & Stroeve, J. 2005, *Virtual sensors: Using data mining techniques to efficiently estimate remote sensing spectra*, IEEE Transactions on Geoscience and Remote Sensing, 43, no. 3

Storchi-Bergmann, T., Kinney, A.L. & Challis, P. 1995, ApJS, 98, 103

Stoughton, C., et al. 2002, AJ, 123, 485

Strauss, M.A., et al. 2002, AJ, 124, 1810

Strateva, I., et al. 2001, AJ, 122, 1861

Suchkov, A.A., Hanisch, R.J., & Margon, B. 2005, AJ, 130, 2439

Vincent, R.A., & Ryden, B. 2005, ApJ, 623, 137

Wadadekar, Y. 2005, PASP, 117, 79

Williams R.E., et al. 1996, AJ, 112, 1335

York, D.G., et al. 2000, AJ, 120, 1579
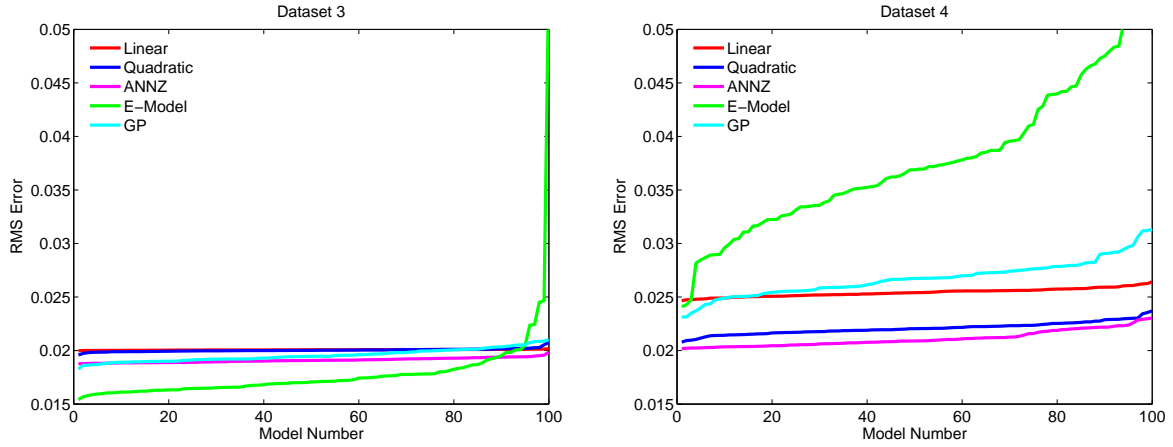
Fig. 5.— Two plots showing the five training methods applied to Datasets 3 (left) and 4 (right).
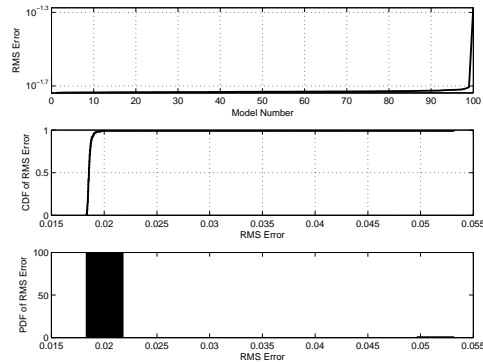
Fig. 6.— The top panel of this figure shows the distribution of errors for 100 neural networks on the GREAT E-Model ugriz-petro50-petro90-qr-fracdev, Dataset 2 (see Table 5). The middle panel shows the empirical cumulative distribution function for the RMS errors for the 100 models shown in the top panel. The bottom panel shows the probability distribution function of the RMS error. See § 5 for more details.
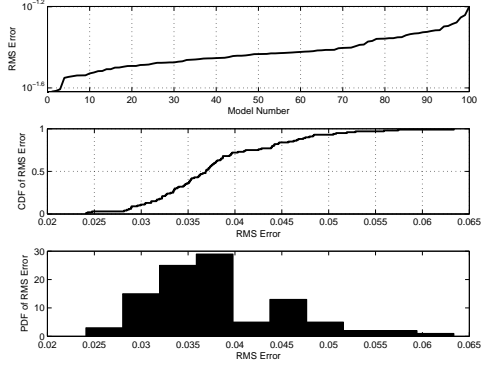
Fig. 7.— The top panel of this figure shows the distribution of errors for 100 neural networks on the GREAT E-Model nuv-fuv-ugriz-jhk, Dataset 4 (see Table 6). The middle panel shows the empirical cumulative distribution function for the RMS errors for the 100 models shown in the top panel. The bottom panel shows the probability distribution function of the RMS error. See § 5 for more details.
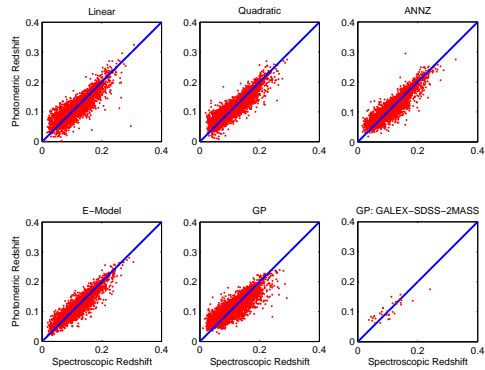
Fig. 8.— Spectroscopic redshift is plotted versus calculated photometric redshift for the GREAT ugriz-petro50-petro90-ci-qr Dataset 2 with 5 algorithms while the 6th plot uses the Gaussian process model for the nuv-fuv-ugriz-jhk GREAT Dataset 4. See Table 4 for details

Table 3: Different Photometric Redshift Techniques and Accuracies.

Method Name	σ_{RMS}	Dataset[1]	Inputs[2]	Source
CWW	0.0666	SDSS-EDR	ugriz	Csabai et al. (2003)
Bruzual-Charlot	0.0552	SDSS-EDR	ugriz	Csabai et al. (2003)
ClassX	0.0340	SDSS-DR2	ugriz	Suchkov et al. (2005)
Polynomial	0.0318	SDSS-EDR	ugriz	Csabai et al. (2003)
Support Vector Machine	0.0270	SDSS-DR2	ugriz	Wadadekar (2005)
Kd-tree	0.0254	SDSS-EDR	ugriz	Csabai et al. (2003)
Support Vector Machine	0.0230	SDSS-DR2	ugriz+r50+r90	Wadadekar (2005)
Artificial Neural Network	0.0229	SDSS-DR1	ugriz	Collister & Lahav (2004)

---

[1]SDSS-EDR Early Data Release (Stoughton et al. 2002), SDSS-DR1 Data Release 1 (Abazajian et al. 2003), SDSS-DR2 Data Release 2 (Abazajian et al. 2004)

[2]ugriz=5 SDSS magnitudes, r50=Petrosian 50% light radius in r band, r90=Petrosian 90% light radius in r band.

Table 4. Photometric Redshift prediction RMS errors with confidence levels for Dataset 1, 202,297 objects

Input-parameters[1]	Linear			Quadratic			ANNz			E-Model			GP		
	(50%)	(10%)	(90%)	(50%)	(10%)	(90%)	(50%)	(10%)	(90%)	(50%)	(10%)	(90%)	(50%)	(10%)	(90%)
ugriz	0.0283	0.0282	0.0284	0.0255	0.0255	0.0255	0.0206	0.0205	0.0208	0.0201	0.0198	0.0205	0.0227	0.0225	0.0230
ugriz+r50+r90	0.0288	0.0288	0.0289	0.0245	0.0244	0.0245	0.0194	0.0192	0.0196	0.0189	0.0187	0.0194	0.0236	0.0233	0.0241
ugriz+r50+r90+CI	0.0286	0.0285	0.0286	0.0264	0.0263	0.0265	0.0194	0.0191	0.0195	0.0187	0.0185	0.0190	0.0239	0.0236	0.0243
ugriz+r50+r90+CI+QR	0.0296	0.0295	0.0296	0.0245	0.0244	0.0246	0.0192	0.0189	0.0194	0.0186	0.0184	0.0190	0.0241	0.0238	0.0245
ugriz+r50+r90+FD	0.0286	0.0286	0.0287	0.0263	0.0261	0.0266	0.0189	0.0188	0.0192	0.0183	0.0181	0.0187	0.0236	0.0233	0.0241
ugriz+r50+r90+FD+QR	0.0290	0.0289	0.0290	0.0243	0.0242	0.0243	0.0189	0.0187	0.0191	0.0185	0.0183	0.0186	0.0239	0.0235	0.0242

[1]ugriz=5 SDSS magnitudes, r50=Petrosian 50% light radius in r band, r90=Petrosian 90% light radius in r band, CI=Petrosian Inverse Concentration Index, FD=FracDev value, QR=Stokes value. See § 3.6 for more details.

Table 5. Photometric Redshift prediction RMS errors with confidence levels for Dataset 2, 33,328 objects

Input-parameters[1]	Linear			Quadratic			ANNz			E-Model			GP		
	(50%)	(10%)	(90%)	(50%)	(10%)	(90%)	(50%)	(10%)	(90%)	(50%)	(10%)	(90%)	(50%)	(10%)	(90%)
ugriz	0.0242	0.0241	0.0242	0.0225	0.0225	0.0225	0.0208	0.0207	0.0209	0.0197	0.0194	0.0200	0.0243	0.0237	0.0248
ugriz+r50+r90	0.0227	0.0227	0.0227	0.0217	0.0216	0.0217	0.0201	0.0199	0.0202	0.0194	0.0192	0.0198	0.0237	0.0232	0.0241
ugriz+r50+r90+CI	0.0240	0.0240	0.0240	0.0226	0.0226	0.0226	0.0200	0.0199	0.0202	0.0192	0.0191	0.0194	0.0242	0.0238	0.0247
ugriz+r50+r90+CI+QR	0.0235	0.0235	0.0235	0.0213	0.0213	0.0213	0.0197	0.0195	0.0198	0.0185	0.0183	0.0189	0.0243	0.0237	0.0255
ugriz+r50+r90+FD	0.0243	0.0243	0.0243	0.0220	0.0219	0.0220	0.0196	0.0195	0.0198	0.0185	0.0183	0.0189	0.0230	0.0226	0.0233
ugriz+r50+r90+FD+QR	0.0234	0.0233	0.0234	0.0220	0.0219	0.0220	0.0194	0.0193	0.0196	0.0185	0.0184	0.0188	0.0242	0.0238	0.0245

[1]ugriz=5 SDSS magnitudes, r50=Petrosian 50% light radius in r band, r90=Petrosian 90% light radius in r band, CI=Petrosian Inverse Concentration Index, FD=FracDev value, QR=Stokes value. See §3.6 for more details.

Table 6. Photometric Redshift prediction RMS errors with confidence levels for Datasets 3 and 4.

Input-parameters[1]	Linear			Quadratic			ANNz			E-Model			GP		
	(50%)	(10%)	(90%)	(50%)	(10%)	(90%)	(50%)	(10%)	(90%)	(50%)	(10%)	(90%)	(50%)	(10%)	(90%)
nuv+fuv+ugriz+jhk[2]	0.0201	0.0200	0.0201	0.0200	0.0199	0.0202	0.0191	0.0188	0.0194	0.0171	0.0161	0.0195	0.0195	0.0189	0.0203
nuv+fuv+ugriz+jhk[3]	0.0254	0.0249	0.0259	0.0220	0.0214	0.0229	0.0209	0.0204	0.0222	0.0369	0.0296	0.0475	0.0267	0.0249	0.0291

[1]ugriz=5 SDSS magnitudes, nuv=GALEX NUV magnitude, fuv=GALEX FUV magnitude, jhk=2MASS jkh magnitudes. See § 3.6 for more details.

[2]Dataset 3: 3095 combined catalog objects

[3]Dataset 4: 326 combined catalog objects